THEORETICAL AND APPLIED MECHANICS
Volume 45 (2018) Issue 2, 205–230 DOI: https://doi.org/10.2298/TAM180415011A

CONSTITUTIVE MODELING FOR FRP COMPOSITE MATERIALS SUBJECT TO EXTREME LOADING

Robert J. Asaro and David Benson

Abstract. A physically based, finite deformation, rate and temperature dependent theory and model have been developed to simulate the deformation and failure of FRP composite materials and structures. Failure modes include: inter alia, fiber crushing and kinking as occurs during extreme compressive loading; fiber fracture as occurs in for example fragmentation; interlaminar shear as occurs at elevated temperatures and that leads to kinking; debonding and delamination including the coupling with laminate kinking; and debonding as occurs in cored FRP panels. The theory/model is capable of describing quasi-static (including creep) as occurs at elevated temperatures, and dynamic deformation and failure as occurs during shock, blast or impact.

The model is implemented within LS DYNA and specific example simulations are described that illustrate the theory/model capabilities. In Part I, fragmentation is not covered in detail. Fiber fracture and fragmentation are to be covered to detail with specific examples in Part II.

1. Introduction

Whereas failure mechanisms in FRP composite are well known via experimental observations and by direct observations of failures that occur in actual applications, the modeling of them has to date been ad-hoc and phenomenological [1, 2]. This has led to what has been recognized as serious limitations on the accuracy and dependability of such modeling and hence to limitations on the reliability of theoretical designs that depend on such modeling. Moreover, the numerical implementation of such models has often times been problematical in that computational efficiency is low and issues of numerical stability are quite common. Moreover, the inclusion of important characteristics of the deformation and failure of FRP composites such as rate sensitivity of deformation and failure are typically not included [1, 2]. Rate effects are, however, of vital importance when dealing with deformations that occur at high rates such as during shock, impact, or blast like loading or during exposure to elevated temperatures that occur during fire or blast. We call loading under such conditions, *extreme loading*.

2010 *Mathematics Subject Classification:* 74D10; 74E30.
Key words and phrases: FRP composite buckling, FRP composite compressive failure.

Herein we present a novel constitutive model describing deformation and failure, including *progressive failure* and material separation, i.e., fragmentation, of laminated FRP composite materials. Our model has evolved over the years through the analysis of failure of FRP composite materials, and complex FRP composite structures, subject to extreme loading via blast, shock, impact, and fire as illustrated in Fig. 1; the particular example shown is that of the failure (i.e., complete breaching) of a composite joint taken from a large ship structure.

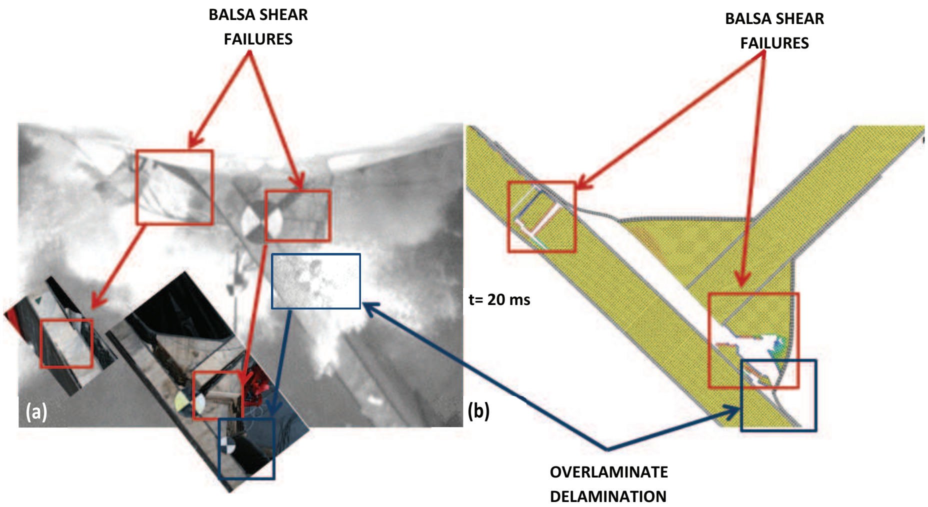

FIGURE 1. Failure of a composite joint extracted from a large ship structure following experimental simulated blast loading at UCSD's Blast Facility. This joint was fabricated from balsa cored carbon-vinylester skin sandwich panels. Note that the failure involves a combination of material failure (i.e., shear in the balsa core) and an important phase of delamination of the *overlayer* within the fillet zone.

Our model includes failure via interlaminar shear (affected by elevated temperature), fiber rupture in tension, fiber crushing (aka kinking) in compression and that also involves interlaminar shear (again as affected by temperature), microcracking, and failure via delamination. Element designs accommodate all types of failure modes. In this we focus on structural failure as influenced by material failure modes such as fiber crushing or kinking that leads to delamination; the affects of core failures are also included. Future extenions will deal with ballistic phenomena, e.g., ballistic penetration, events that involve fiber rupture. Specifically, future analysis will extend the analysis contained herein by examining subsequent effects of fiber rupture whether caused by ballistic loading per se or the intense stresses caused by progressive structural collapse.

The development of this model has paid special attention to eliminating issues of numerical instability and to providing for computational efficiency; benchmarks of such are provided in the discussions. The model is readily implemented in well known FEM codes such as LS DYNA and ABAQUS as described, and demonstrated, below.

Our developments specifically realize the deficiencies in models currently in use and that include, inter alia,

(1) No satisfactory FRP failure models for design use that simulate penetration exist at present; the sort of computational analysis required to simulate failure in FRP composites is both computationally costly and numerically challenging.
(2) Phenomenological models often contain large numbers of ad-hoc "adjustable" parameters that have no clear physical meaning and are very costly in time and money to determine with confidence. It is often unclear how to physically interpret the various terms within these ad-hoc models as they are not based on clear physical observations.
(3) Current FRP composite progressive failure models are numerically inefficient and often display numerical instability.
(4) Important physical aspects of FRP composite material deformation and failure such as rate sensitivity are not included; most all existing models idealize deformation and failure as rate independent. An example of the rate dependence of FRP composite material failure is shown in the load vs. time histories of Fig. 2 following the tests depicted in Fig. 3.

As an example of rate effects, Fig. 2 shows how failures via delamination are affected by loading rate. The failures in this case were observed in experimental tests such as shown in Fig. 3. These tests subjected balsa cored short sandwich beams, with carbon/vinyester skins, to bending at various loading rates as shown and sketched in Fig. 3.

Our model development addresses all these deficiencies and others as explained throughout the text. In particular, the second of the two example simulated cases described below in Section 4 deals directly with material defect driven local failures that lead to faceskin/core delamination.

2. Background & general perspectives on composite failure

Among the great impediments to the use of FRP composites in the design and construction of high performance structures, such as ship and aircraft structures, are their susceptibility to degradation due to exposure to the elevated temperatures caused by fire and the as yet inability to assess damage to them caused by the dynamic loading due to blast, shock, or impact. During exposure to fire FRP materials degrade through the direct loss of material by ablation and char formation, as well as simply by exposure to elevated temperatures in the range of say, $60\,^{\circ}\mathrm{C} < T < 125\,^{\circ}\mathrm{C}$. Losses in material strength result from such exposures while the materials are at these temperatures and they undergo losses even after the materials are returned to ambient temperatures. Residual material properties fare better and for FRP material systems currently proposed for use for load bearing structures, residual properties can be maintained at near 100 % even after exposures

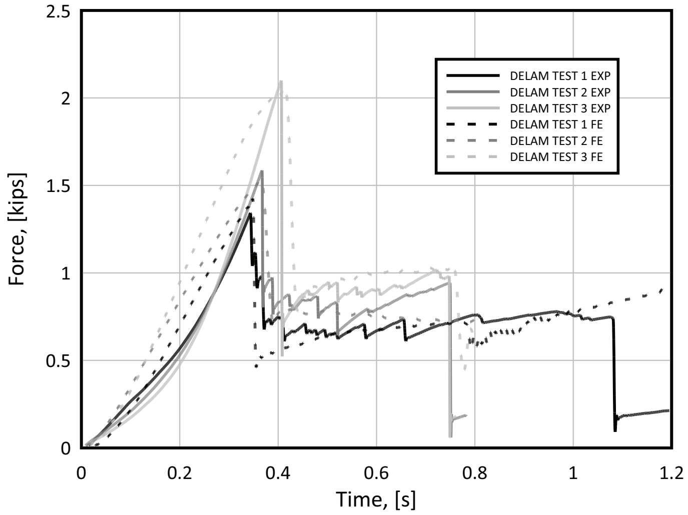

FIGURE 2. Failure of a composite balsa cored carbon fiber beam at various loading rates that span an induced strain rate range of 10^{-2}–$10^{2}\,\mathrm{s}^{-1}$. Failures in this case were primarily due to delamination. Note that not only are the reaction forces affected by loading rate, but also the failure time, i.e., the failure progression, is affected as well.

to temperatures of up to 200 °C. When subject to impact or blast loading FRP composite materials undergo damage, and consequent degradation of their properties, via mechanisms that include, inter alia, interlamellar delamination within skins or at laminate/core interfaces, laminate failure through kinking or fiber crushing, or fracture. Assessment of the behavior and response of FRP composite materials is therefore required to allow for adequate design and risk assessment vis-à-vis threat scenarios consistent with blast and/or fire induced damage. A constitutive framework is therefore required for describing the elastic-viscoplastic response of FRP materials to dynamic loading such as due to blast, and to the elevated temperatures of fire, that can be used, in turn, to analyze the observations of material behavior during laboratory testing and that can be used to perform full-scale structural analyses of structures. Herein we present such a constitutive framework.

The framework described herein was guided by the dual needs of developing a theory that could embody the phenomenology of material loss as well as degradation in properties of intact material, yet be analytically tractable and computationally efficient to allow for engineering design. The material model would is hence amenable to implementation along with the co-developed algorithms being describing property degradation and/or phase transformations as occur during material ablation. It was envisioned that the theory would have a relatively straightforward implementation in standard finite element codes and thus serve as a useful tool for the assessment of material damage and structural response.

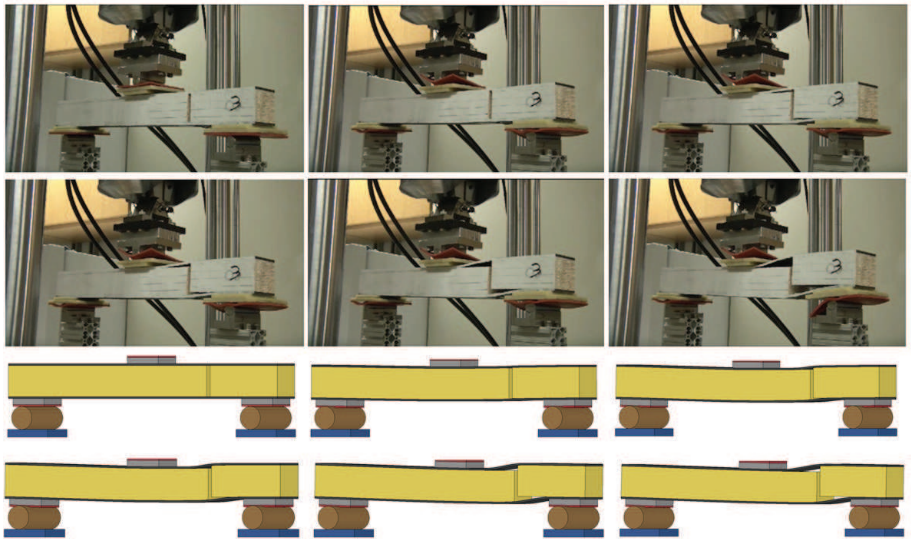

FIGURE 3. Bend tests of a composite balsa cored carbon fiber beam at various loading rates that span an induced strain rate range of 10^{-2}–$10^{2}\,\mathrm{s}^{-1}$. Failures in this case were primarily due to delamination. Note that failure is initially induced via balsa core shear that *then* leads to delamination of the face skin/core interface. After delamination, skin laminate rupture may occur leading to complete breach, i.e., separation, of the assembly.

Figure 4 shows examples of typical failure modes found in FRP composites subject to high compressive stress. Figures 4a,b show examples of structural buckling and delamination. What is noteworthy, however, it that even though the most prominent feature of Figs. 4a,b are the obvious delamination, the cause of failure itself may not be apparent in the post failure images at all. On the one hand, delamination leads to severe losses in buckling resistance and load carrying capacity. On the other hand, delamination may be caused by the large compressive stresses that result from compressive buckling, i.e., delamination may well be a result of a structural buckling failure and not the primary cause of it. Still an additional possibility is that delamination may have resulted from a more local material failure mode such as the kinking shown in Fig. 4c. Such local material failures-that result from high compressive stresses-also result in losses in global stiffness, that in turn induce global response such as buckling. *Thus what was clear is that a theory was required that captures the complete gambit of all such phenomena so that their important interactions are fully accounted for in a rigorous and consistent manner.*

In many of its aspects, our new theory borrows from the successful development of the theory for crystal plasticity, especially as laid out by Asaro (1977, 1985) [**3**, **4**], and Harren and Asaro (1989) [**5**]; specific citations in context are given where appropriate in the text. The theory will account fully for the anisotropy

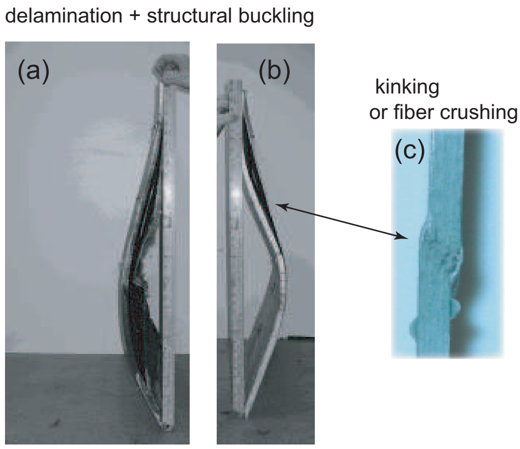

FIGURE 4. Typical compressive failure modes for FRP composite laminates and panels. (a) and (b) show examples of global buckling of FRP panels subject to compressive loads (Asaro *et al.* 2007), where delamination is evident. (c) shows an example, courtesy of Prof. J. Lesko, Virginia Technical University, of a local material failure via kinking in a single laminate "skin", caused by applied compressive loading [9]. Note that local material failure mechanisms such as kinking, seen in (c), affect global stiffness and global response as seen in (a) and (b). Such local $\leftrightarrow$ global mode interactions make it necessary to incorporate both levels of phenomenology into a consistent physically based theory.

of FRP laminate elastic behavior as well as for the highly anisotropic inelastic response that occurs due to interlaminar shear. The latter process is strongly influenced by temperature and strain rate. As noted above, there was the very real need for computational efficiency and this has led us to avoid constructing a discrete aggregate model, which while attractive in its ability to separately describe the roles of polymer matrix and fabric, would inevitably lead to a far more computationally expensive implementation that would render performing (many) engineering design simulations inviable. The framework for constructing such models, in fact, already exists as the need may arise and a particularly relevant foundation lies in the cell models recently proposed by Gu and Asaro [11]. On the other hand, we present here an explicit algorithm for the numerical integration of the theory within a finite element framework that is both stable and highly efficient.

As noted above, of particular interest is the ability to describe common *failure mechanisms* that occur in FRP materials. Along with general elastic-viscoplastic deformation at elevated temperature these are seen to arise particularly as a result of compressive loading. One such failure mode is *micro-buckling* or *kinking*, which typically leads to rapid, often localized, degradation and fracture (e.g., as in the examples shown in Fig. 4). We desired, therefore, a theory that naturally contains the occurrence of such phenomena. The model need also contain an accurate description of the temperature dependence of material stiffness and material resistance to interlaminar shear-these were, accordingly, key focuses of our development.

The plan of the paper is as follows. In the next section notations and conventions are defined. Background on our physically based model follows along with a more detailed kinematical scheme upon which the theory is based. The theory is laid out in subsequent sections. Our integration algorithm is described. Material calibration using experimental data taken from past work concerned with quasi-static and high rate deformation of FRP panels is described to add further perspective and to provide detailed calibration of the constitutive parameters. Two specific example simulations are given that include failures due to extreme dynamic compressive loading; the second of which includes superimposed bending arising from the imposition of lateral pressure, say as arising from blast of impact.

3. Constitutive & failure model

3.1. Nomenclature & conventions. Standard notations are used throughout. Bold-faced symbols are used to denote vectors and higher order tensors, the order of which will be clear in context. Products are indicated with dots or double dots, which denote summation over repeated Latin or Greek indices, and products without dots are dyadic products. Latin indices range from one to the number of spatial dimensions (usually three), and repeated Latin indices are always summed. However, indices that are within parentheses are not summed. Inverses, transposes, and transpose inverses are denoted with a superscripted -1, T, and $-T$, respectively, and superposed dots indicate differentiation with respect to time, t. For instance,

$$\begin{aligned}
&\mathbf{A}\cdot\mathbf{B} = A_{ik}B_{kj}\mathbf{b}_i\mathbf{b}_j, && \mathbf{A}:\mathbf{B} = A_{ij}B_{ji}, && \mathbf{cd} = c_i d_j \mathbf{b}_i\mathbf{b}_j,\\
&\mathbf{c}\cdot\mathbf{d} = c_i d_i, && \mathbf{H}:\mathbf{A} = H_{ijkl}A_{lk}\mathbf{b}_i\mathbf{b}_j, && \mathbf{A}:\mathbf{H} = A_{kl}H_{lkij}\mathbf{b}_i\mathbf{b}_j,\\
&\dot{\mathbf{B}} = \frac{\partial B_{ij}}{\partial t}\mathbf{b}_i\mathbf{b}_j, && \mathbf{B}\cdot\mathbf{c} = B_{ik}c_k\mathbf{b}_i, && \frac{\partial \mathbf{c}}{\partial \mathbf{d}} = \frac{\partial c_i}{\partial d_j}\mathbf{b}_i\mathbf{b}_j.
\end{aligned}$$

where the base vectors $\mathbf{b}$ are Cartesian and independent of time. Greek indices are *slip system* identifiers ranging from one to four for the case of an orthotropic laminate such as considered herein and as explained below. In the above we represent tensor products as, for instance, $\mathbf{ab}$ or $\mathbf{AB}$ rather than use the familiar $\otimes$ symbol as in $\mathbf{a}\otimes\mathbf{b}$.

3.2. The laminate model: background. The basic kinematics is illustrated in Fig. 5. We consider the FRP material to be composed of an essentially orthotropic laminate, and to contain a sufficient number of plies so that homogenization is a reasonable way to describe the material behavior.[1] The principal directions of the fibers are described by a set of mutually orthogonal unit base

[1]The homogeneous view taken here is, on the other hand, not necessary and it is indeed possible to apply the theory developed here on a "ply-by-ply" level. In a finite element model separate elements may be used for each ply along with the use of cohesive elements at the interlamellar layers. The latter would be a logical way to describe intralamellar delamination if desired.

vectors, $\mathbf{a}_i$, as depicted in Fig. 5. The resulting orthotropic elastic response of the laminated composite will, thus, be fixed on, and described by these vectors. The material can also deform via slipping in the plane of the laminate, i.e., via *interlaminar shear*, and this slipping is confined to this interlaminar plane. Slipping is possible in all directions in the plane, but not necessarily with equal ease. We thus introduce two slip systems aligned with the *slip directions* $\mathbf{s}_1$ and $\mathbf{s}_2$. The normal to the laminate plane is $\mathbf{m}$, and clearly $\mathbf{s}_1 \cdot \mathbf{m} = 0$ and likewise $\mathbf{s}_2 \cdot \mathbf{m} = 0$. It may well be natural, but not necessary, to take $\mathbf{s}_1$ and $\mathbf{s}_2$ to be orthogonal, i.e., $\mathbf{s}_1 \cdot \mathbf{s}_2 = 0$, but note that due to elastic distortions they may not remain so during deformation. These vectors will be called $\mathbf{s}_1^*$, $\mathbf{s}_2^*$, and $\mathbf{m}^*$ in the deformed state, but since $\mathbf{m}^*$ is to be the normal to the slip plane, i.e., the plane of the laminate, it will always be the case that $\mathbf{s}_1^* \cdot \mathbf{m}^* = 0$ and $\mathbf{s}_2^* \cdot \mathbf{m}^* = 0$ as shown to be naturally described by

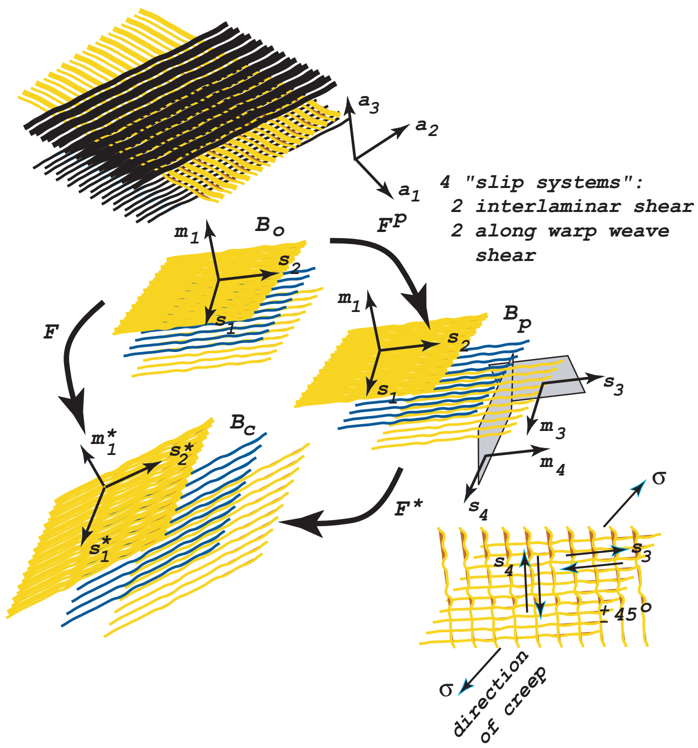

FIGURE 5. Kinematics of deformation. Note, the total deformation as prescribed by $\mathbf{F}$ is decomposed into a process of interlaminar shear followed by an elastic deformation of the orthotropic framework. Rigid body deformations are described in $\mathbf{F}^*$, the deformation gradient of the framework. The base vectors a_i are defined on the laminate itself and thus rotate and deform with the laminate. For this illustration thermal deformation is not included.

our expressions for the kinematics of laminate deformation. In fact, it is possible to take the slip system vectors to be coincident with the laminate base vectors, $\mathbf{a}_i$ and insure that they are convected so that the above stated orthogonality is preserved; there is no need to do this however. Even though both slip systems have the same slip plane normal, i.e., $\mathbf{m}$, it will be convenient for symmetry of expression to refer to $\mathbf{m}_1$ and $\mathbf{m}_2$ in the expressions below. This makes it easier to establish correlations with the body of theory for crystal plasticity.

We next introduce two additional slipping systems, labeled 3 and 4 as shown at the lower right corner of Fig. 5. The slip planes are oriented perpendicular to the laminate plane and along the fiber directions; this is illustrated by the planes whose normals are $\mathbf{m}_3$ and $\mathbf{m}_4$. The slip directions, that lie along the fiber directions, are $\mathbf{s}_3$ and $\mathbf{s}_4$, respectively. These systems are what we refer to as the *warp-weave* shearing systems. Note that $\mathbf{m}_3 \cdot \mathbf{m}_1 = \mathbf{m}_3 \cdot \mathbf{m}_2 = 0$, and likewise $\mathbf{m}_4 \cdot \mathbf{m}_1 = \mathbf{m}_4 \cdot \mathbf{m}_2 = 0$. Calibration of the properties of the warp-weave systems relies on measurements of creep response and is generally done as a function of temperature as described below.

3.3. The laminate theory. The thermo-elastic-viscoplastic response of the laminate is described using the kinematical scheme as shown in Fig. 6. The undeformed, stress free, laminate represents the reference configuration. Each material particle is described by its reference position vector, $\mathbf{X}$. The α^{th} slip system of the

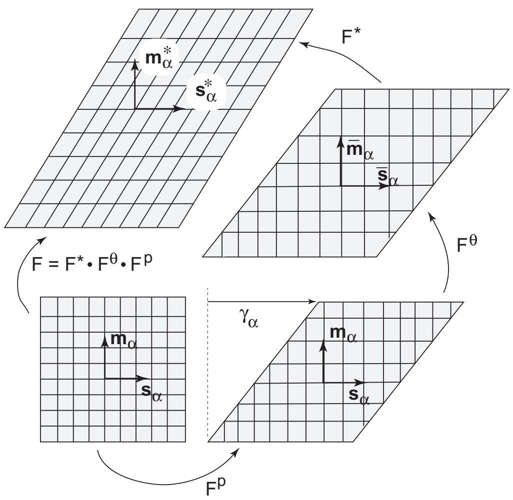

FIGURE 6. Kinematics of deformation. Note, the total deformation as prescribed by $\mathbf{F}$ is decomposed into a process of interlaminar shear followed thermal and then an elastic deformation of the orthotropic framework. Rigid body deformations are described in $\mathbf{F}^*$, the deformation gradient of the framework. The base vectors a_i are defined on the laminate itself and thus rotate and deform with the laminate.

laminate is described by the orthogonal pair of unit vectors $\mathbf{s}_\alpha, \mathbf{m}_\alpha$; $\mathbf{s}_\alpha$ is aligned with the α^{th} shear direction and $\mathbf{m}_\alpha$ is the unit normal to the α^{th} slip plane in the reference configuration. The plastically, thermally, and elastically deformed laminate represents the current configuration. In the current configuration each material particle is described by its current position vector, $\mathbf{x}$. The current configuration is described by the deformation gradient $\mathbf{F} = \partial \mathbf{x}/\partial \mathbf{X}$. In order to reach the current configuration from the reference configuration, we imagine first that material flows through the undeformed laminate via shears along the various slip systems-as described just above-to reach the first intermediate configuration which is described by the plastic deformation gradient, $\mathbf{F}^p$. The spatial velocity gradient of these shears is written as

$$\dot{\mathbf{F}}^p \cdot \mathbf{F}^{p-1} = \dot{\gamma}_\alpha \mathbf{s}_\alpha \mathbf{m}_{(\alpha)}, \tag{3.1}$$

where $\dot{\gamma}_\alpha$ is the shearing rate on the α system. From this plastically deformed state the second intermediate configuration is reached by imagining the laminate undergoing deformation due to temperature change, described by the thermal deformation gradient, $\mathbf{F}^\theta$, where θ represents temperature. The spatial velocity gradient for this is written as

$$\dot{\mathbf{F}}^\theta \cdot \mathbf{F}^{\theta-1} = \dot{\theta}\boldsymbol{\alpha}; \quad \boldsymbol{\alpha} = \alpha_{ij}\mathbf{a}_i\mathbf{a}_j. \tag{3.2}$$

$\boldsymbol{\alpha}$ is a tensor whose components, α_{ij}, with respect to time-independent Cartesian laminate base vectors, $\mathbf{a}_i$, are thermal expansion coefficients. These base vectors are aligned with the laminate planes and slip directions in those planes in the reference configuration, e.g., the slip directions are aligned in a physically meaningful way with the fiber directions. This would of course render the matrix of thermal expansion coefficients in the simplest of forms.

The current, i.e., the deformed, configuration is reached by elastically distorting the laminate and rigidly rotating it, along with the embedded material, which is described by the elastic deformation gradient, $\mathbf{F}^*$. Hence one has the total deformation gradient

$$\mathbf{F} = \mathbf{F}^* \cdot \mathbf{F}^\theta \cdot \mathbf{F}^p. \tag{3.3}$$

In reality, the elastic distortion of the laminate, thermal deformation, and inelastic-i.e., interlamellar and/or warp-weave shearing-occur simultaneously, but it is nonetheless clear that the current configuration of this model can be reached by the above described sequence of events. For a concise presentation of the remaining development, we combine deformation gradient parts as follows: we define

$$\hat{\mathbf{F}} = \mathbf{F}^\theta \cdot \mathbf{F}^p, \quad \bar{\mathbf{F}} = \mathbf{F}^* \cdot \mathbf{F}^\theta. \tag{3.4}$$

The driving force for slipping on the α slip system is defined as

$$\tau_\alpha = \mathbf{m}^*_\alpha \cdot \boldsymbol{\tau} \cdot \mathbf{s}^*_\alpha; \quad \mathbf{s}^*_\alpha = \bar{\mathbf{F}} \cdot \mathbf{s}_\alpha; \quad \mathbf{m}^*_\alpha = \mathbf{m}_\alpha \cdot \bar{\mathbf{F}}^{-1}; \quad \boldsymbol{\tau} = J\boldsymbol{\sigma}, \tag{3.5}$$

where $J = \det\{\mathbf{F}\}$ is the Jacobian determinant of the deformation gradient, $\boldsymbol{\tau}$ is the Kirchhoff stress, and $\boldsymbol{\sigma}$ is the Cauchy stress. In eq. (3.5), $\mathbf{s}^*_\alpha$ is along the α^{th} slip direction in the current configuration and $\mathbf{m}^*_\alpha$ is normal to the α slip plane in the current configuration. As discussed by Hill and Rice [13], Asaro and Rice [3], or more recently by Asaro [12], τ_α is defined as above to make it conjugate to $\dot{\gamma}_\alpha$, i.e., so that in fact $\tau_\alpha \dot{\gamma}_\alpha$ is the inelastic dissipation rate per unit reference volume.

The constitutive description of the inelasticity on each "slip system" is cast in terms of the resolved shear stress and slip rate on that system as

$$\dot{\gamma}_\alpha = \dot{a}\,\mathrm{sgn}\{\tau_\alpha\}\left\{\left|\frac{\tau_{(\alpha)}}{g_{(\alpha)}}\right|\right\}^{1/m}, \tag{3.6}$$

where τ_α and g_α are the current values of the resolved shear stress and slip system "hardness" (i.e., strength), respectively. In eq. (3.6), m is the rate sensitivity exponent and $\dot{a} > 0$ is a reference shear rate, both of which are the same for each slip system; sgn($\cdot\cdot$) means the "sign" of $\{\cdot\cdot\}$. Usually it is sufficient to take the material parameters m and $\dot{a}$ to be constants in fitting experimental data. Note that as $m \to 0$, rate independent behavior is achieved so that, in this limit, g_α may be identified with the current slip system strength, τ_α. In the general case, for $m \neq 0$, g_α is the current slip system strength when shear occurs on the slip system at its reference rate, $\dot{a}$.

The slip system hardness, g_α, is treated as an integral variable whose current value is obtained by the path dependent integration of the evolution equation

$$\dot{g}_\alpha = h_{\alpha\beta}(\gamma_\alpha, \theta)|\dot{\gamma}_\beta| + g^\theta_\alpha(\gamma_\alpha, \theta)\dot{\theta}; \quad \gamma_\alpha = \int_0^t \sum_\alpha |\dot{\gamma}_\alpha|\,\mathrm{d}t, \tag{3.7}$$

where $h_{\alpha\beta}$ is a matrix of (non-negative) hardening moduli, g^θ_α is the rate of change of slip system hardness with respect to temperature alone, and γ_α is the accumulated sum of slips (aka the *accumulated slip*). γ_α increases monotonically for any, even non-monotonic, inelastic loading history and it is similar to the accumulated *effective plastic strain* used in flow theories. The initial conditions for this evolution are specified as $g_\alpha(\gamma_\alpha = 0, \theta = \theta_0) = g_0(\theta_0)$, where θ_0 is an initial temperature.

As regards the thermal deformation, the α_{ij} are regarded as being constant, i.e., are unaffected by either deformation or temperature change. It is important to point out that in this formulation the material temperature distribution and the thermal history are considered to be externally prescribed and are not affected by the deformation; for example, the effects of inelastic dissipation on temperature are not incorporated. Still another way of saying this is: the thermal and mechanical processes are taken as decoupled.

The description of the laminate's response is completed by specifying its elasticity. The stress, $\mathbf{S}^*$ in the laminate depends solely on the laminate distortion of its plys, which is expressed in terms of its Green strain, $\mathbf{E}^*$. These quantities are written as

$$\mathbf{E}^* = \tfrac{1}{2}(\mathbf{F}^{*T} \cdot \mathbf{F}^* - I); \quad \mathbf{S}^* = F^{*-1} \cdot \boldsymbol{\tau} \cdot F^{*-T}, \tag{3.8}$$

where S^* is the laminate based second Piola-Kirchhoff stress-conjugate to $\mathbf{E}^*$, so that $S^* : \dot{\mathbf{E}}^*$ is the rate of laminate distortional energy per unit reference volume- and $\mathbf{I}$ is the second order identity tensor. The elastic response is written as

$$S^*_{ij} = \frac{\partial \mathbf{\Phi}}{\partial E^*_{ij}}; \quad \mathbf{S}^* = S^*_{ij} a_i a_j; \quad \mathbf{E}^* = E^*_{ij} a_i a_j, \tag{3.9}$$

where $\mathbf{\Phi} = \mathbf{\Phi}(E^*_{ij})$ is the Hemholtz free energy of the laminate per unit reference volume.[2] In rate form we have

$$\dot{\mathbf{S}}^* = \mathbf{K} : \dot{\mathbf{E}}^*; \quad \mathbf{K} = K_{ijkl} a_i a_j a_k a_l; \quad K_{ijkl} = \frac{\partial^2 \mathbf{\Phi}}{\partial E^*_{ij}\, \partial E^*_{kl}}. \tag{3.10}$$

This allows the material's anisotropy to be fully accounted for. Note that the kinematics of the model follow quite naturally the planes of the plys and thus allow for a ready description of interlamellar events such as delamination.

The entire constitutive theory can be described by a governing rate form. The Lagrangian description is chosen, which involves the second Piola-Kirchhoff stress, $\mathbf{S}$ and the Green strain, $\mathbf{E}$ defined as

$$\mathbf{S} = \mathbf{F}^{-1} \cdot \boldsymbol{\tau} \cdot \mathbf{F}^{-T}; \quad \mathbf{E} = \tfrac{1}{2}(\mathbf{F}^T \cdot \mathbf{F} - \mathbf{I}), \tag{3.11}$$

where both are proper conjugate variables. To derive the governing rate form one begins by differentiating the first of eq. (3.8) with respect to time to obtain an expression for $\dot{\mathbf{E}}^*$. Next one substitutes eq. (3.3) into the second of eqs. (3.11) and differentiates the result with respect to time to obtain an expression for $\dot{\mathbf{E}}$. Combining the expressions for $\dot{\mathbf{E}}^*$ and $\dot{\mathbf{E}}$ and using eqs. (3.1) and (3.2) yields

$$\dot{\mathbf{E}}^* = \hat{\mathbf{F}}^{-T} \cdot \dot{\mathbf{E}} \cdot \hat{\mathbf{F}}^{-1} - \dot{\gamma}_\alpha \mathbf{A}_\alpha - \dot{\theta}\mathbf{B} \tag{3.12a}$$

$$\mathbf{A}_\alpha = \mathrm{sym}\{\mathbf{F}^{*T} \cdot \mathbf{F}^* \cdot \mathbf{F}^\theta \cdot (\mathbf{s}_\alpha \mathbf{m}_{(\alpha)}) \cdot F^{\theta-1}\} \tag{3.12b}$$

$$\mathbf{B} = \mathrm{sym}\{\mathbf{F}^{*T} \cdot \mathbf{F}^* \cdot \boldsymbol{\alpha}\}, \tag{3.12c}$$

which expresses the additive decomposition of the strain rate on the second intermediate configuration, i.e., the total strain rate is equal to the elastic strain rate plus the plastic strain rate plus the thermal strain rate. Next combining eq. (3.3), the second of eqs. (3.8) and the first of eqs. (3.11) it becomes clear that

$$\mathbf{S}^* = \hat{\mathbf{F}} \cdot \mathbf{S} \cdot \hat{\mathbf{F}}^T. \tag{3.13}$$

After differentiating this with respect to time and combining with eqs. (3.1) and (3.2) we find that

$$\dot{\mathbf{S}}^* = \hat{\mathbf{F}} \cdot \dot{\mathbf{S}} \cdot \hat{\mathbf{F}}^T + 2\dot{\gamma}_\alpha \mathbf{H}_\alpha + 2\dot{\theta}\mathbf{Q} \tag{3.14a}$$

$$\mathbf{H}_\alpha = \mathrm{sym}\{\mathbf{F}^\theta \cdot (\mathbf{s}_\alpha \mathbf{m}_{(\alpha)}) \cdot \mathbf{F}^{\theta-1} \cdot \mathbf{S}^*\} \tag{3.14b}$$

$$\mathbf{Q} = \mathrm{sym}\{\boldsymbol{\alpha} \cdot \mathbf{S}^*\} \tag{3.14c}$$

which expresses the connection between the two stress rates on the second intermediate configuration, i.e., the stress rate is equal to the elastic stress rate minus a softening due to inelastic deformation and thermal strains. Note that $g(\gamma_\alpha, \theta)$ is also the slip system hardness in the case of isotropic latent hardening. Finally, the governing constitutive rate form is obtained by substitution of eq. (3.12a) and

[2] We note that alternatively the laminate's elasticity may be specified via a standard "laminate theory" that would then result in the elastic constant tensor as noted in the text.

(3.14a) into eq. (3.10), yielding

(3.15a) $$\dot{\mathbf{S}} = \mathbf{L} : \dot{\mathbf{E}} - \dot{\gamma}_\alpha \mathbf{X}_\alpha - \dot{\theta}\mathbf{Y}$$

(3.15b) $$L_{ijrn} = \hat{F}^{-1}_{ik}\hat{F}^{-1}_{jl}K_{klpq}\hat{F}^{-1}_{rp}\hat{F}^{-1}_{nq}$$

(3.15c) $$\mathbf{L} = L_{ijkl}\mathbf{a}_i\mathbf{a}_j\mathbf{a}_k\mathbf{a}_l; \quad \hat{\mathbf{F}}^{-1} = \hat{F}^{-1}_{ij}\mathbf{a}_i\mathbf{a}_j$$

(3.15d) $$\mathbf{X}_\alpha = \hat{\mathbf{F}}^{-1} \cdot \mathbf{R}_\alpha \cdot \hat{\mathbf{F}}^{-T}; \quad \mathbf{R}_\alpha = \mathbf{K} : \mathbf{A}_\alpha + 2\mathbf{H}_\alpha$$

(3.15e) $$\mathbf{Y} = \hat{\mathbf{F}}^{-1} \cdot \mathbf{Z} \cdot \hat{\mathbf{F}}^{-T}; \quad \mathbf{Z} = \mathbf{K} : \mathbf{B} + 2\mathbf{Q}.$$

Given the current state, $\mathcal{S} = \{\mathbf{S}^*, \mathbf{E}^*; \mathbf{F}^p, \mathbf{F}^\theta, g_\alpha\}$, which is described by both state variables and internal variables, one obtains the slipping rates, $\dot{\gamma}_\alpha$, unambiguously from eq. (3.6). The state $\mathcal{S}$ also unambiguously specifies the tensors $\mathbf{L}$, $\dot{\gamma}_\alpha\mathbf{X}_\alpha$, and $\mathbf{Y}$ so that eq. (3.15a) provides an incrementally linear relation between $\dot{\mathbf{S}}$ and $\dot{\mathbf{E}}$. Use of linear elasticity means that the K_{ijkl} are invertible, since inelasticity is incompressible we have $\det(\mathbf{F}^p) = 1$ and for finite thermal expansion coefficients it can be shown that $\det(\mathbf{F}^\theta) > 0$ so that the tensor $\mathbf{L}$ is invertible. Hence, the relation between $\dot{\mathbf{S}}$ and $\dot{\mathbf{E}}$ is always invertible ensuring uniqueness of solutions to mixed boundary value problems within the context of this theory.

3.4. Fiber degradation & failure. Fiber, or fabric, response and primarily in tension is taken to be linear elastic up to a critical strain, ϵ_c, as indicated in Fig. 7. At ϵ_c and at larger strains the fiber, or fabric, stiffness degrades according to the curve labeled (2) in the figure. Eventually the fibers, or fabric, lose all stiffness (i.e., break). Residual degradation is also modeled as indicated by the dashed line, that is upon unloading and reloading the stiffness is reduced by the damage envisioned to have occurred.

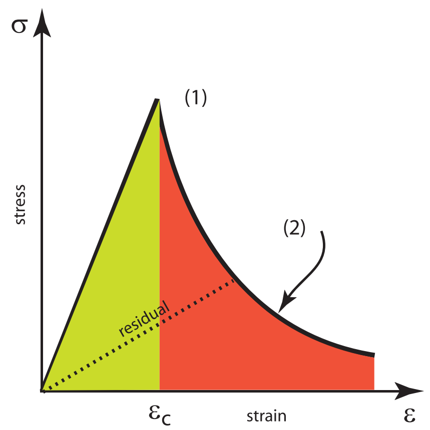

FIGURE 7. Fibers, or fabric, are modeled as linear elastic up to a point of a critical strain as indicated by point (1). Thereafter their stiffness is degraded as indicated by curve (2). Note that residual stiffness is also modeled as indicated by the dashed line so labeled.

As noted in the Introduction, Section 1, fiber fracture is to be fully implemented in Part II of this series and thus will be detailed there. This brief description is for perspective only.

3.5. Decohesion of composite laminates and interfaces. There are several forms of composite decohesion (aka delamination) that are vital in the process of structural failure. One, illustrated in Figs. 1 and 2, involves the separation of laminate skins from structural cores; interestingly in both cases the delamination was triggered by structural core shear failure. A second is the delamination of individual plys as illustrated in Fig. 4c.

3.6. Numerical implementation. The numerical implementation uses backward Euler to integrate the second Piola-Kirchhoff stress rate form in Eq. (3.15a),

$$\mathbf{S}^{n+1} = \mathbf{S}^n + \triangle t(\mathbf{L} : \dot{\mathbf{E}} - \dot{\gamma}_\alpha(\mathbf{S}^{n+1})\mathbf{X}_\alpha) \tag{3.16}$$

where Eq.s (3.5) through (3.7) are used to express the inelasticity and the hardness evolution through the updated stress on the right hand side. The thermal contribution in Eq. (3.15a) is handled through operator splitting in a separate thermal step, and the temperature is treated as constant during the mechanical time step. The resulting system of six nonlinear algebraic equations with residuals $\mathbf{R}(\mathbf{S}^{n+1})$

$$\mathbf{R}(\mathbf{S}^{n+1}) = \mathbf{S}^{n+1} - \mathbf{S}^{\text{trial}} + \triangle t\dot{\gamma}_\alpha(\mathbf{S}^{n+1})\mathbf{X}_\alpha = 0 \tag{3.17}$$

are solved using full Newton iteration. The "trial" terminology is borrowed from the radial return approach to integrating J_2 plasticity equations with backward Euler,

$$\mathbf{S}^{\text{trial}} = \mathbf{S}^n + \triangle t\mathbf{L} : \dot{\mathbf{E}}. \tag{3.18}$$

3.7. Calibration of the constitutive model. To account for the loss in material stiffness at elevated temperatures we will take the degradation in properties to be described by a master degradation function for all components of moduli, namely one that is monotonically decreasing with increasing temperature. This means that in eq. (3.20) $K_{ijkl} \leftarrow f(T)K_{ijkl}$, where $f(T)$ is the monotonically decreasing function shown in the figure. It should be possible to improve on this simple representation of stiffness degradation with further experimental study of the effect of temperature on anisotropic stiffness. Losses in shear strength are handled, again as a first step in our modelling, by replacing $g(\gamma_a)$ in eq. (3.6) with $\eta(\gamma_a)$, where $\eta = r(T)g(\gamma_a)$. The function $r(T)$ is to be determined by experimental documentation of the effect of temperature on the resistance to interlaminar shear. Thus, the shearing rates are calculated from,

$$\dot{\gamma}_\alpha = \dot{\gamma}_0 sgn\{\tau_\alpha\}\left\{\left\|\frac{\tau_\alpha}{\eta_\alpha}\right\|\right\}^{1/m}, \tag{3.19}$$

In the examples shown in the next section $r(T)$ is taken to be of the same general monotonically decreasing form as $f(T)$.

In general, orthotropic elastic symmetry is presumed although the materials will often possess transverse isotropy. Thus the elastic constants will have components, when phrased on the orthotropic axes of the form,

$$\mathbf{K} = K_{ijkl}\mathbf{a}_i\mathbf{a}_j\mathbf{a}_k\mathbf{a}_l. \tag{3.20}$$

If the common convention of index contraction is used, i.e., $11 \leftrightharpoons 1$, $22 \leftrightharpoons 2$, $33 \leftrightharpoons 3$, $23, 32 \leftrightharpoons 4$, $13, 31 \leftrightharpoons 5$, and $12, 21 \leftrightharpoons 6$, the matrix of components becomes,

$$\begin{Bmatrix} K_{11} & K_{12} & K_{13} & 0 & 0 & 0 \\ K_{12} & K_{22} & K_{23} & 0 & 0 & 0 \\ K_{13} & K_{23} & K_{33} & 0 & 0 & 0 \\ 0 & 0 & 0 & K_{44} & 0 & 0 \\ 0 & 0 & 0 & 0 & K_{55} & 0 \\ 0 & 0 & 0 & 0 & 0 & K_{66} \end{Bmatrix}$$

the elements of this stiffness matrix may be formed directly from experimental measurement of the elastic moduli, or from standard laminate theory.

To determine values for the reference shear strain rate $\dot{\gamma}_0$, the initial and final flow stresses (g_0 and g_∞, respectively), the initial hardness modulus h_0 and the strain rate sensitivity exponent m_{srs}; a multiparameter optimization was performed using a computational implementation of this material model to match experimental creep data obtained via Professor J. Lesko at Virginia Tech. The experimental values were for a biaxial e-glass vinylester composite, subject to creep when loaded in in-plane tension at a 45° from both initial fiber directions, and took the form of normalized warp-weave shear strain vs. time curves measured at a variety of temperatures; the temperature of 90 °C only was used for the current purpose. The optimization was performed over all five variables simultaneously using an implementation of the Nelder–Meade Simplex Algorithm, together with penalty functions to keep parameters within what were deemed reasonable bounds. The algorithm was run over a grid of ninety-seven initial value combinations. The values thus determined were $\dot{\gamma}_0 = 1.81 \times 10^{-6}$, $g_0 = 0.0386$ MPa, $g_\infty = 6.63$ MPa, $h_0 = 6950$, and $m_{\mathrm{srs}} = 0.0727$. The optimum fit is shown in Fig. 8. In fact, the fit is not ideal; this is due to the fact that the general hardening function used is unable to accurately represent this phenomena-a better analytic form for the hardening function should be determined. Further note that the interlaminar response has not

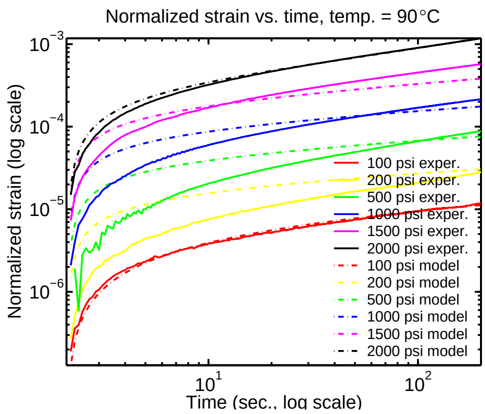

FIGURE 8. Creep data curve-fitting. Data taken from Boyd et al. [9].

been measured directly-however the warp-weave properties are used for these slip directions as well because they represent the best available data. To estimate the shear degradation function $r(T)$, a simplified optimization was repeated for temperatures 30 °C, 60 °C, 90 °C, and 110 °C. The degradation of these parameters was found to closely follow the line $r(T) = -0.00787T + 1.157$, insofar as $0 < r(t) \leqslant 1$.

4. Examples: dynamic panel response

We consider two examples of compressive deformation of sandwich panels, one with superimposed bending, as example applications of the constitutive model. The examples are specifically chosen to illustrate the ability of the model to predict failure modes such as kinking and the interaction of local modes such as kinking on global response. We note, as discussed above, that with degradation due to elevated temperatures, interlaminar shear, i.e., slip, is induced and this will lead to an early onset of failure modes such as kinking. Of course, other failure modes such as *skin wrinkling* are also likely to be triggered and these will compete with failure modes such as *structural buckling* and kinking. Our constitutive and numerical framework is capable of describing all these modes, as they compete, en toto. In the present examples, however, we will focus on kinking as described in the first example below. The examples illustrate, however, the occurrence of faceskin/core debonding as triggered by kinking. In our second example we augment the failure scenario with the occurrence of core shear failure triggered by superposed bending, the bending caused by transverse pressure as would occur via shock and/or impact, or via blast overpressure.

4.1. Kinking/debonding of sandwich composite skin. Our first example is designed to illustrate the phenomena of kinking and thus is based on a particular geometry that isolates the phenomena. Specifically, we analyze a short i.e., “stubby” laminate loaded compressively. The stubbiness makes global buckling occur at loads much higher that those required for kinking. As kinking is primarily influenced by interlaminar shear, we do not anticipate an important influence of creep, i.e., warp-weave shear, in this first example. This, as it happens, was observed.

4.1.1. *Problem description.* The sandwich is taken to be symmetric and consists of a relatively compliant core (balsa wood) and skins of symmetric lay-up with respect to the mid-plane of the sandwich, held together by an adhesive layer. In the particular case examined, the core is 50 mm thick, and the skins are of 1.75 mm thickness. Figure 9 shows a schematic view and the finite element mesh and helps to explain the model. The specimen is further taken to be 100 mm tall, and is modeled with plane-strain constraint in the y direction (into the plane of the drawing) with one layer of solid hexahedral 8-noded finite elements. Only one half is discretized as symmetry is assumed. It is noted here, and below, that the specimen is purposely taken to be “stubby” so as to effectively preclude the appearance of structural buckling. This is done so that the appearance of kinking modes, that are inherent in the theory, would be highlighted. As discussed below, when more slender specimens are analyzed, kinking modes would compete with structural buckling modes and indeed a typical specimen, or structure, would display combinations of such modes; such is the case in Example # 2.

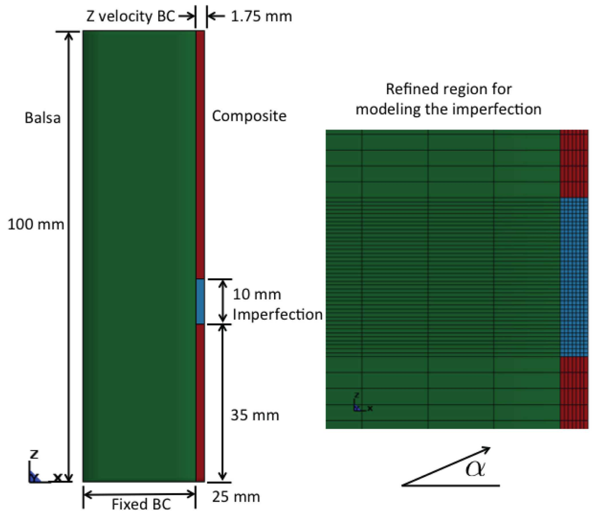

FIGURE 9. View of the overall geometry and the zoom-in of the imperfection area. The balsa core and the carbon/vinylester skins are 25 mm and 1.75 mm thick, respectively. Note the imperfection in laminate orientation, α. This stubby specimen has an aspect ratio of 2.

The core is modeled as an isotropic elastic material although full anisotropic laminate geometry is included. The constitutive model outlined above is used for the skin of the composite with slip plane normal parallel in the reference configuration, viz. the x-direction, to the surface of the skin. There is, however, a *geometrical imperfection* in the slip plane normal at about the midpoint of the panel. In particular, between $z = 35\,\text{mm}$ and $z = 45\,\text{mm}$, the orientation of the laminate, and thus the slip plane normal, is assumed to deviate from the x direction by an angle α. The imperfection, characterized by the angle α, is shown in the insert to Fig. 9.[3]

When the specimen is subjected to compression in the z direction, we therefore expect to see kink(s) formed in the skin(s) of the sandwich composite. The core and skins are held together by a single layer of thin elements, designed to replicate the adhesive layer. These elements have properties designed to simulate the debonding of the skin once the maximum strength of the adhesive (or tensile strength of the core) is reached. In particular, when the positive principal stress value exceeds a given limit, the element's internal stress is assigned a zero value, thus effectively deactivating the quadrature point. This limiting decohesive stress is $\sigma_{\max} = 1\,\text{MPa}$.

4.1.2. *Material Parameters.* For computational economy, in this example, only the center part ($35\,\text{mm} < z < 65\,\text{mm}$) of the specimen skin is elasto-viscoplastic; other parts of the skin are assumed to remain (hyper-) elastic. The constitutive parameters of the skin material are as follows: elastic constants are $c_{11} = 204\,000\,\text{MPa}$,

[3]The imperfection is a section of laminate that is misaligned with the z-direction by angle α. Most typically such imperfections involve wavy laminate; the angle α is taken as constant here.

$c_{12} = 68\,000\,\mathrm{MPa}$, $c_{44} = 68\,000\,\mathrm{MPa}$, (implying isotropy), isotropic or Taylor hardening parameter $q = 1$, initial hardening rate $h_0 = 1$, reference shear strain rate $\gamma_0 = 300$, initial flow stress $g_0 = 27\,\mathrm{MPa}$, saturation strength $g_{\mathrm{inf}} = 30\,\mathrm{MPa}$, strain-rate sensitivity exponent $m_{\mathrm{srs}} = 0.05$, material density $\rho = 1.6 \times 10^{-9}\,\mathrm{ton\,m^{-3}}$. Note that it has been assumed that the skins are elastically isotropic for the example shown.

The core is elastic, and the material parameters are as follows: Young's modulus $E = 17\,000\,\mathrm{MPa}$, Poisson's ratio $\nu = 0$, material density $\rho = 0.6 \times 10^{-9}\,\mathrm{ton\,m^{-3}}$. The adhesive layer elements are assigned a tensile cut-off strength of 1 MPa.

4.1.3. *Initial and Displacement Boundary Condition.* The top surface is made to move downwards at various rates, v, with velocities in the range $25\,\mathrm{mm\,s^{-1}} \leqslant v \leqslant 400\,\mathrm{mm\,s^{-1}}$ with the bottom surface of the specimen fixed in the z direction. Therefore, the initial condition is a linearly interpolated velocity distribution in the z direction. This corresponded to imposing a nominal compressive strain rate, $\dot{\epsilon}$, in the range $0.25\,\mathrm{s^{-1}} \leqslant \dot{\epsilon} \leqslant 4.0\,\mathrm{s^{-1}}$.

A plane-strain constraint is applied in the y direction, and the skins at the top and bottom portions of the model are prevented from moving in the x direction to prevent global buckling mode of failure. We note that, in general, global buckling is a failure mode that competes with kinking. We preclude it here, by our choice of geometry, because we are more interested at this point at examining the phenomenology of materials, rather than structural, failure modes. The latter are examined in our second example.

We note at this point that the formation of a kink within the faceskin involves the development of large tensile normal stresses across the faceskin/core interface; this is anticipated to lead to debonding of that interface. Moreover, as the kink develops the fibers within it are subject to large tensile strains that eventually lead to fiber fracture and thereby to fragmentation. Although not covered in this Part I, as noted above, this will lead to complete failure beyond the stages described herein.

4.1.4. *Results.* The results are reported in several ways. First we show the essential phenomenology of kink formation leading to delamination and then show the effects of imposed rate and imperfection details on this behavior.

In Fig. 10a the deformed mesh is shown at a time of 0.004 s, that corresponds to a peak load of approximately 930 N. The imposed top edge velocity in this simulation was $v = 100\,\mathrm{mm\,s^{-1}}$ which corresponded to a nominal deformation rate $\dot{\epsilon} = 1.0\,\mathrm{s^{-1}}$. In Fig. 10a the plot is of the bottom half of the specimen; complete views of the specimen are shown in Fig. 11. It is clear that a kink has formed that, in turn, leads to large tensile stress at the skin/core interface; this then leads to debonding as is evident in the figure.

The process of kinking and structural degradation is affected by imposed deformation rate as shown in Fig. 10b. As the deformation rate increases the peak load also increases as well as the time to acquire peak loading. This a direct result of the rate dependence of inelastic interlamellar shearing due to the strain rate dependence of interlamellar inelastic deformation described via flow laws such as given by eq. (3.6). The observation that the peak load increases with compressive deformation rate reflects the rate dependence of interlamellar shear strength as embodied

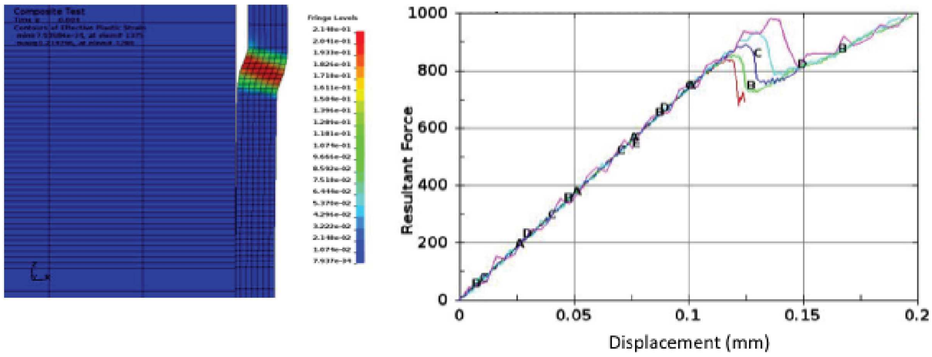

FIGURE 10. (a) Deformed mesh for the case where the upper boundary velocity was $v = 100\,\mathrm{mm/s}$ and the imperfection angle $\alpha = 7°$. The peak load at this point was about 930 N and occurred at a time of 0.004 s. The effect of the imperfection is to cause fiber kinking that then led to debonding of the faceskin/core interface. (b) Peak force vs. displacement for various upper boundary velocities of 25, 50, 100, 200, and 400 mm/s for curves A through E, respectively. Note the relationship of peak force vs. deformation rate reflecting the strain rate dependence of interlamellar inelastic shear vs. strain rate.

in the rate rule of eq. (3.6). Indeed, kinking essentially occurs coincidentally with interlamellar inelastic shear. This is also reflected in the dependence of peak load on imperfection angle, α, as discussed next.

The effect of imperfection angle, α, on "kink band $\rightsquigarrow$ faceskin/core debond phenomenology" is shown in Fig. 11; the simulations involved here are for a compressive deformation rate of $\dot{\epsilon} = 1.0\,\mathrm{s}^{-1}$. Figure 11 contains full specimen contours of effective plastic strain for 5 values of α, viz., $\alpha = 1.25°, 2.5°, 5°, 7.5°, 10°$ as viewed from left to right; the fringe scales are shown in the lower left corner of the figure. It is noteworthy that as the imperfection angle becomes larger the kink becomes more localized in the sense that the zone of intense inelastic shear becomes more spatially confined. Moreover, as α increases, the resultant faceskin/core debonding is shifted more to one side of the imperfection, viz., atop it.

The resulting force vs. displacement, at fixed rate, is also affected by imperfection angle as shown in Fig. 12; from this we extract the effect of imperfection angle, α, on peak force. The peak forces follow a relationship that may be fitted to the relation

$$L_{\max} \approx 4.75 \times 10^3 \left\{ \frac{\sin(2\alpha_0)}{\sin(2\alpha)} \right\}^{0.8}, \tag{4.1}$$

where $\alpha_0 = 1.25°$. This fit is approximate, nearly linear in the ratio $\sin(2\alpha_0)/\sin(2\alpha)$, but is consistent with the observation that kinking, and peak load, occur coincidentally with achieving a critical resolved shear stress on the laminates within the "imperfect" region. This is so since the resolved shear stress, call it τ, on a plane,

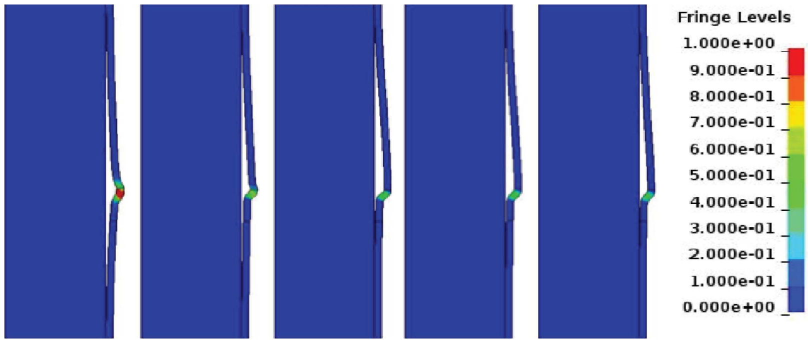

FIGURE 11. Effect of imperfection angle, α, on kink formation. The imposed deformation rate for all cases shown here was $\dot{\epsilon} = 1.0\,\mathrm{s}^{-1}$. Figures from left to right show contours of effective plastic strain for case where $\alpha = 1.25°$, $2.5°$, $5.0°$, $7.5°$, $10.0°$. Scale bar at lower right is of effective plastic strain.

(i.e., the laminate slip plane) inclined at angle α to the direction of uniaxial compression is given by

$$\tau = \tfrac{1}{2}\sin(2\alpha)\sigma, \tag{4.2}$$

with σ being the compressive stress. Thus, if the onset of kinking in such cases as described in this simulation is coincident with the onset of inelastic shearing within the laminates, then we expect such a nearly linear inverse relation between peak load (i.e., stress) and $\sin(2\alpha)$.

Finally, we note that the peak displacement at peak force is also affected by imperfection angle as shown in Fig. 13. This shows what should at this point be an

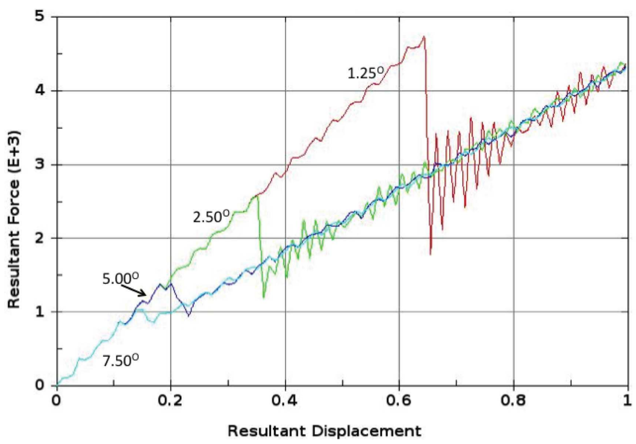

FIGURE 12. (a) Force vs. displacement as affected by imperfection angle, α.

expected trend of decreasing maximum compressive displacement with imperfection angle; given eq. (4.2) it seems plausible that it would take a lower overall compressive strain to reach a critical value of load and hence τ to trigger interlamellar shear and thus kinking.

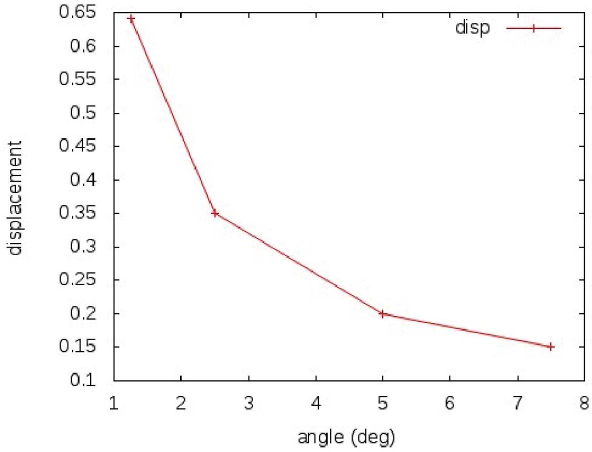

FIGURE 13. Peak displacement vs. α for the cases shown in Figs. 11 and 12.

An important perspective to gain, however, is that although the onset of such phenomena such as fiber crushing and kinking may set limits to maximum load bearing capacity, the ultimate response, and progression of failure, of a FRP composite structure is determined by a complex sequence of subsequent deformation/failure events. It is thus necessary to simulate a more complete sequence of events as our next example demonstrates.

4.2. Structural failure as influenced by core shear induced kinking and debonding. In this second example, a model of a sandwich panel is developed and analyzed both with and without elastic-viscoplastic behavior, to demonstrate the critical role viscoplastic microbuckling (shear kinking) plays in the development of global structural failure. As noted in the first example, interlaminar shear induced kinking is caused by critically high interlaminar shear stresses due to initial fiber misalignments present within the composite. These initial imperfections are known to be present, and indeed have been measured and statistically characterized for carbon fiber composites (see e.g., Yurgartis, 1987 [10]). Thus a model without such imperfections does not completely represent a realistic material description that must include inevitable manufacturing defects. This example will show that in cases where kinking is a contributing failure mode (as is common in compressively loaded composites), a failure to fully represent the material physics that lead to kinking will, in turn, lead to significantly incorrect results. The case to be presented is, in fact, one in which a local mode such as kinking directly interacts with a global mode, viz. structural buckling. In addition, we include the possibility of core shear failure, a mode that is common in sandwich panels subjected to bending. Bending is induced via imposed transverse pressure, simulating either impact or shock wave (e.g., blast) loading.

As noted in Fig. 1 and also in Fig. 3, as examples, structural failure often initiates as a material failure such as core shear that then leads to debonding and loss of all structural integrity. In this example we demonstrate how multiple material failure modes such as core shear couples to laminate kinking that, in concert, lead to interface seperation and complete global structural failure. This, therein, demonstrates the utility of our constitutive model and our overall approach.

4.2.1. *Problem description.* A full sandwich panel is modeled, see Fig. 14a, implementing our material model with an initial fiber misalignment in one skin. The span (i.e., height) is now larger than used in Example #1 and is set at 200 mm; the core 12.69 mm, and the skins 3.56 mm in thickness. This more slender geometry allows for a bending mode of deformation essentially precluded in our first example. In the finite element mesh, eight-node hexahedral finite elements are used. The solution is achieved via a dynamic relaxation method for convenience of implementation. For computational economy, again only the center portion ($92 < z < 108$ mm) of the specimen skin is elastic-viscoplastic; other parts of the skin are assumed to remain elastic. The constitutive parameters of the skin material are as follows: elastic constants are $c_{11} = 204\,000$ MPa, $c_{12} = 68\,000$ MPa, $c_{44} = 68\,000$ MPa, (implying isotropy), isotropic or Taylor hardening parameter $q = 1$, initial hardening rate $h_0 = 3130$, reference shear strain rate $\gamma_0 = 5.36 \times 10^{-8}$, initial flow stress $g_0 = 0.296$ MPa, saturation strength $g_\infty = 6.03$ MPa, strain-rate sensitivity exponent $m_{srs} = 0.0454$, material density $\rho = 1.6 \times 10^{-9}$ ton m^{-3}.

The imperfection in laminate orientation, placed in the first skin of the panel, is of the same type as in our first example. The imperfection is a section in which the laminates are misaligned with the vertical, i.e., the z-direction, by an angle α. As compression is applied in the z-direction, the imperfection is essentially removed by setting $\alpha = 0$, at least under pure uniaxial compression; the loading here is, however, a combined compression+ bending. The core is elastic, and its material parameters are as follows: Young's modulus $E = 1700$ MPa, Poisson's ratio $\nu = 0$, material density $\rho = 0.6 \times 10^{-9}$ ton m^{-3}. An adhesive layer is present between the core and the first skin, and its elements are assigned a tensile cut-off strength of 1 MPa. In addition, we allow for core shear failure along a line triggered when the shear stress attains a critical value, $\tau_{\mathrm{crit}} = 1.0$ MPa. The general region most likely to undergo core shear failure is indicated in Fig. 14a.

4.2.2. *Initial and Displacement Boundary Conditions.* The model is subject to plane-strain boundary conditions in the y direction (i.e., it is one element layer in depth). As in example # 1, a downward velocity, v, is imposed on the top edge (see Fig. 14c). A bending moment is induced via the imposition of a ramp of transverse pressure, $p(t)$, also indicated in Fig. 14c. This moment is initially zero, then is ramped up to a maximum level and held constant; it has the general form

$$p(t) = \begin{cases} \beta t, & t \leqslant t_f \\ \beta t_f = p_{\max}, & t > t_f. \end{cases} \tag{4.3}$$

In this example $p_{\max}$ is set at xxx N. Two cases are discussed in detail here, one where $\alpha = 0°$ (i.e., no imperfection) and where $\alpha = 5°$.

4.2.3. *Results.* Figures 14b,c show specimen snapshots at specific times, *viz.* $t = 0.001$ s and $t = 0.0002$ s for the cases where $\alpha = 0°$ and $\alpha = 5°$, respectively. The overall, i.e., global, specimen response is clearly, and remarkably, different without and with an imperfection. In both cases, core shear failure occurs essentially injecting a shear/opening mode crack onto the core/skin interface. However, the defining effect of the imperfection is to induce kinking and a dramatic loss in bending stiffness. The specimen then undergoes collapse followed by extensive core/skin debonding. In contrast, without the imperfection the specimen retains bending stiffness and structural integrity despite the presence of the obvious core shear/opening mode crack (which is, of course, transverse to the specimen's span).

Additional perspective is gained vis-à-vis the specimen's global response by following the specimen's transverse displacement, i.e., d as defined in Fig. 14c; this is shown in Fig. 15. With an imperfection, and as suggested by Fig. 14c, the specimen is driven to collapse. Without an imperfection, the specimen undergoes a vibratory transverse motion while continuing downward compression. At least under the boundary conditions used here, the specimen is far from collapse during the times considered. With $\alpha = 5°$, the structural failure of the panel is thus essentially catastrophic. With values of α in the range $0 < \alpha \leqslant 5°$, collapse still occurs albeit at longer times and larger net compressive deflections.

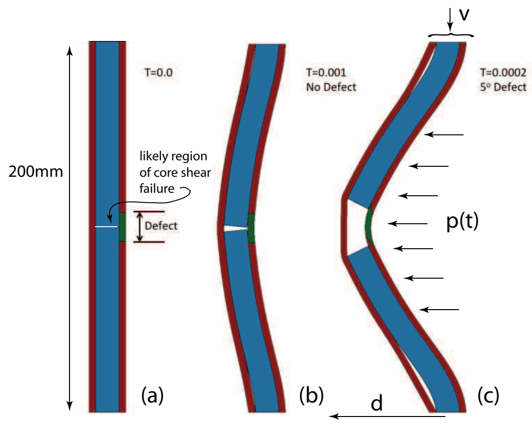

FIGURE 14. Example 2: (a) A full panel is modeled with one skin containing a geometrical imperfection as described for example # 1; the imperfection, i.e., defect, described by angle α is located in one skin as indicated. (b), with $\alpha = 0°$ and at time $t = 0.001$ s, and (c), with $\alpha = 5°$ and $t = 0.0002$ s, show the specimen after being subjected to a compressive velocity of $v = 100\,\mathrm{mm\,s^{-1}}$ and a transverse pressure of $p(t)$ described in the text. Note that a shear crack formes across the core in all cases; the likely region of such cracks is indicated in (a).

To explore the effect of imperfection severity, simulations were carried out with imperfections in the range $0 \leqslant \alpha \leqslant 5°$; the results for transverse deflection are also shown in Fig. 15. As noted in that figure, with $\alpha = 1.25°$ the specimen is seen to collapse albeit at longer times. Between $\alpha = 1.25°$ and $\alpha = 0°$, the specimen's transverse response becomes vibratory and for the durations considered avoids catastrophic collapse. Thus the structural response is quite sensitive to imperfection severity. It may indeed be the case that the structural response is sensitive to imperfection type as well.

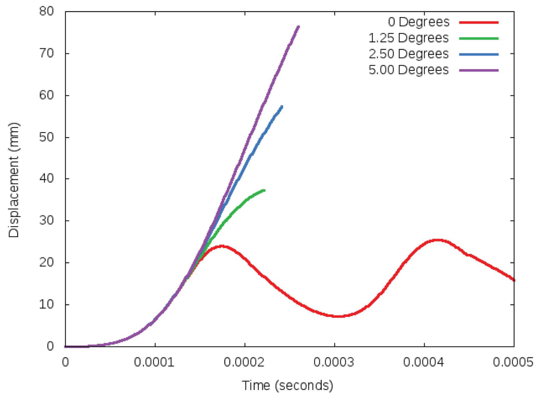

FIGURE 15. Example 2: Lateral displacement vs. time for cases with various imperfections, $0 \leqslant \alpha \leqslant 5°$.

5. Discussion and conclusions

The examples shown above were chosen to illustrate the versatility of our physically based theory/model and, in particular, the important interplay between local "material-like" failure modes such as skin crushing or kinking and global response. For these purposes the boundary conditions were chosen to highlight critical phenomenology that are driven by such localized material failure modes. Clearly, the inclusion of realistic descriptions of material structure, such as laminate perfection, is vital as demonstrated via Example #2. This, in fact, highlights a significant benefit of our physically based kinematics. Calibration of ad-hoc FRP composite failure models as reviewed in [1, 2] would be not merely prohibitively expensive in terms of financial burden and time for experimental calibration, but unreliable as such calibration would be on a "case-by-case" basis for every different material encountered and each particular scenario. Our approach, on the other hand requires a relatively simple set of experimental calibrations that are then used to simulate a quite wide range of scenario's.

Example #2 requires a bit more discussion. In actual loading scenario's (i.e., loading events), that may occur for example during blast, shock, or impact, imposed motions and/or forces are typically transient. Considering this, we might well reassess the results shown in Fig. 14 as follows. Without an imperfection, and for event durations of say less than $1 - 3$ms, the specimen may have been judged to have survived. The presence of a material defect, however, alters this assessment considerably; in fact, the specimen and hence the structure would be judged to have failed, globally. *This is not a mere difference of degree, but a difference in deciding failure or no failure!* The salient point here is that anticipating failure modes-as complex as they are in FRP composites-and "rigging" ad-hoc constitutive models in attempts to reproduce them is destined to be neither reliable nor viable given the variability of failures modes and patterns. Fiber rupture leading to fragmentation is an interesting and hence intriguing next step.

Carrying this discussion further, as we intend in Part II of this report, we would then ask about the subsequent events triggered by fiber rupture. Fiber rupture would, indeed, be expected at points where the local tensile stresses are extreme and this, in turn, would be expected at sites of extreme laminate bending at kinks and regions of sever bending. Even a cursory examination of Figs. 14b,c would be sufficient to expect that with defects accounted for, as in Fig. 14c, there is far more likelihood of fiber rupture, and hence more accurate prediction of it by accounting for material defects. Fiber rupture is to be initially modeled using a simple critical tensile stress criterion as depicted in Fig. 7. Although ad-hoc, such a criterion is credible for such fibers that are essentially linear elastic until undergoing brittle-like fracture.

References

1. M. J. Hinton, P. D. Soden, *Predicting failure in composite laminates: the background to the exercise*, Composite Science and Thechnology **58** (1998), 1000–1010.
2. M. J. Hinton, A. S. Kaddour P. D. Soden, *A comparison of the predictive capabilities of current failure theories for composite laminates, judged against experimental evidence*, Compos. Sci. Tech. **62** (2002), 1725–1797.
3. R. J. Asaro, J. R. Rice, *Strain localization in ductile single crystals*, J. Mech. Phys. Solids **25** (1977), 309–338.
4. R. J Asaro, A. Needleman, *Texture development in rate dependent polycrystals*, Acta Met. **27** (1985), 45–65.
5. S. V. Harren, R. J. Asaro, *Nonuniform deformation in polycrystals and aspects of of the validy of the Taylor model*, J. Mech. Phys. Solids **37** (1989), 191–232.
6. R. J. Asaro, P. Krysl, B. Zhu, W. T. Ramroth, *Rate dependent constitutive modeling of laminated FRP composites by fire*, Compos. Struct. **68** (2005), 399–408.
7. R. J. Asaro, P. Huson, L. Stewart, G. A. Hegemier, *Non-explosive methods for simulating blast loading of structures with complex geometries*, Int. J. Impact Eng. **38**(7) (2011), 546–557.
8. A. Chen, H. Kim, J. Bezares, R. J. Asaro, *Non-explosive simulated blast loading of balsa core sandwich composite beams*, Compos. Struct. **93**(11) (2011), 2768–2784.
9. S. E. Boyd, J. V. Bausano, S. W. Case, J. J, Lesco, *Mechanistic approach to structural fire modeling of composites*, in *Modeling of Naval Composite Structures in Fire*, L. Couchman, AP Mouritz eds., Acclaim Publishing Services, Templestowe, Victoria, Australia, 2006.
10. S. W. Yurgartis, *Measurement of small angle fiber misallignments in continuous fiber composites*, Compos. Sci. Tech. **30** (1987), 279–293.
11. P, Gu, R. J. Asaro, *Structural buckling of polymer matrix composites due to reduced stiffness from fire damage*, J. Compos. Struct. **69** (2004), 65-75.
12. R. J. Asaro, *Crystal plasticity*, J. Appl. Mech. **50** (1983), 921–934.
13. R. Hill, J. R. Rice, *Constitutive analysis of elastic-plastic crystals at arbitrary strain*, J. Mech. Phys. Solids **20** (1972), 401–413.

КОНСТИТУТИВНО МОДЕЛОВАЊЕ FRP КОМПОЗИТНИХ МАТЕРИЈАЛА КОЈИ ПОДЛЕЖУ ЕКСТРЕМНОМ ОПТЕРЕЋЕЊУ

Резиме. Развијен је физички заснован модел коначних деформација који зависи од брзине и температуре ради симулације оштећења FRP композитних материјала и структура. Врсте оштећења укључују између осталог: дробљење влакана и увијање које се јавља приликом екстремног оптерећења; прелом влакана која се јавља, на пример, при фрагментацији; интерламинарно смицање на повишеним температурама и које доводи до увијања; одвајање и раслојавање укључујући везу са ламинатним увијањем; растакање као у шупљим FRP панелима. Теорија/модел је у могућности да опише квази-статичку деформацију (укључујући и пузање) на повишеним температурама, као и динамичку деформацију и оштећење који се јављају током ударца, експлозије или удара.

Модел се имплементира у LS DYNA и описани су конкретни примери симулација који илуструју валисност теорије/модела. У првом делу фрагментација није детаљно обухваћена. Прелом влакана и фрагментација са специфичним примерима разматра се детањније у другом делу.

Department of Structural Engineering
University of California
San Diego
La Jolla
USA

(Received 15.04.2018)
(Available online 07.09.2018)